Sensors and Materials, Vol. 36, No. 9 (2024) 4061–4075
MYU Tokyo

S & M 3784

Airborne Bathymetric Light Detection and Ranging Waveform Processing for Digital Elevation Model Construction of Tidal Flats on the West Coast of Korea

Hyejin Kim[1] and Jaebin Lee[2*]

[1]Social Eco-Tech Institute, Konkuk University, Gwangjin-gu, Seoul 05029, South Korea
[2]Department of Architectural, Civil, and Environmental Engineering, Mokpo National University, Muan, Jeonnam 58554, South Korea

(Received August 29, 2024; accepted September 20, 2024)

Keywords: airborne bathymetric LiDAR, DEMs, tidal flats, shallow and turbid water, waveform processing

Digital elevation models (DEMs) are essential for quantitatively monitoring the current state and changes in the morphology of tidal flats and extracting terrain information, such as tidal channels. However, the unique environmental characteristics of tidal flats, where water and land coexist in shallow areas, make it challenging to apply traditional direct surveying methods or ship-based echo sounding. Additionally, remote sensing technologies such as airborne topographic light detection and ranging (LiDAR), drone photogrammetry, and satellite imagery are challenging to use in submerged areas. Airborne bathymetric LiDAR (ABL), which is capable of directly surveying the seabed through seawater, is a highly effective method for surveying tidal flats. However, the high turbidity and shallow water environment of tidal flats attenuate the return strength, resulting in a low signal-to-noise ratio and making airborne bathymetric LiDAR (ABL) full-waveforms extremely complex. In this study, we aim to improve the performance of ABL full-waveform processing to generate high-precision DEMs in such challenging environments. First, we analyze the characteristics of ABL waveforms under varying turbidity conditions and propose preprocessing and waveform decomposition techniques to improve seabed point extraction rates in tidal flat environments. To achieve this, experiments and validations are conducted using the data acquired by the Seahawk system along the west coast of Korea.

1. Introduction

Intertidal tidal flats occupy at least 127921 km^2 (124286–131821 km^2, 95% confidence interval) worldwide and are characterized by soft sediments that are exposed at low tide. Tidal flats serve as habitats for diverse marine life, act as buffers against marine disasters, including typhoons and tsunamis, and are reservoirs of marine resources and natural filtration systems.(1) As one of the most efficient primary producers in coastal ecosystems, tidal flats can address the

*Corresponding author: e-mail: lee2009@mokpo.ac.kr
https://doi.org/10.18494/SAM5350

ISSN 0914-4935

current biodiversity-climate crisis and contribute to carbon neutrality, climate resilience, biodiversity support, and human well-being.[2] The west coast of Korea is renowned for its extensive tidal flats, which have developed owing to significant tidal variations and the generally flat terrain. These tidal flats, designated as a UNESCO World Heritage site, "Getbol", hold significant ecological importance.[3] However, the total area of Korea's tidal flats has decreased by approximately 22.5% over 30 years, from 3203.5 km² in 1987 to 2487 km² in 2018, owing to land reclamation and other factors.[4] This continuous reduction underscores the increasing need for conservation and management and the importance of conducting accurate surveys of tidal flats and collecting high-precision spatial data to monitor changes.

Among various spatial data, digital elevation models (DEMs) are fundamental for quantitatively monitoring the current state and changes in morphology. They are also highly useful for extracting geomorphic features, such as tidal creeks, and modeling temporal changes using tide models. However, applying traditional direct surveying or ship-based multi-beam echo sounder (MBES) surveying methods in Korea's west coast tidal flats is difficult owing to the water–land environment, significant tidal variations, and shallow depths. The tidal flats stretch along the coastal regions of Korea, with notable tidal ranges of approximately 7.3 m in Incheon, which is located centrally, and approximately 3 m in Mokpo, situated in the southern part of the coast.[5] Over the last decade, remote sensing has demonstrated its potential to address the challenges posed by this difficult environment, with multiple studies conducted using satellite imagery involving the DEM construction of large areas at various timescales.[6–9] Using satellite imagery for DEM construction over large tidal flat areas is effective, but it has limitations, such as low resolution and fixed revisit cycles, making it challenging to survey areas submerged during tidal activities. Recent studies have reported the use of drone imagery[10–12] and airborne light detection and ranging (LiDAR)[13,14] to construct high-resolution DEMs for the tidal flats on the west coast of Korea. However, these methods are limited by the restricted survey ranges and gaps in coverage for areas that remain submerged during surveys. These environmental characteristics considerably enhance the applicability of airborne bathymetric LiDAR (ABL), which uses green lasers and can penetrate the water surface to directly measure the seabed. Specifically, bottom- and surface-water signals are typically detected using ABL systems (more commonly known as full-waveform ABL systems) using the 532 and 1064 nm bands that can detect these signals, respectively.[15] To identify echo types and extract the temporal positions of these echo signals, full-waveform data processing methods are primarily applied.[16] Generally, the in-water transmission of the laser generated by the ABL system is extremely complex, which means that a more complex LiDAR bathymetry modeling is required to compensate for factors such as water surface reflection and refraction, water volume scattering, and turbidity. These factors can complicate the propagation models and attenuate the return intensity, resulting in a lower signal-to-noise ratio (SNR).[17] Tidal flats are particularly challenging for this system owing to continuous tidal activity and the presence of soft sediments, leading to shallow depths and high turbidity. Limited water depths, significant turbidity, and low reflectance impose challenges for bathymetric LiDAR, especially in land–water transition zones where the water surface, water column, and benthic layer returns interact. However, the performance of full-waveform ABL in shallow and turbid waters has received little attention in

the literature except for a few studies.[17–19] In this study, we aim to present a bathymetric full-waveform processing strategy that accounts for unclear bottom return and excessive noise in the tidal environment, thus enabling a more accurate bathymetry determination and the construction of high-precision DEMs in challenging environments using ABL systems.

The remainder of the paper is organized as follows. In Sect. 2, we describe the test site and data used in our experiments. In Sect. 3, we provide a detailed explanation of the proposed method. In Sect. 4, we present the experimental results and evaluations as well as the discussion. In Sect. 5, we conclude with a summary and final remarks.

2. Materials

2.1 Test sites

To verify the bathymetric performance of the proposed approach in the tidal flat area, we selected the west coast of the Korean Peninsula as the test site, where the water depth is less than 2 m and the turbidity is high. Figure 1 and Table 1 show the location and Seahawk observation area of the test site. The test data were collected in the Hwang-do tidal flat in Taean-gun, Chungcheongnam-do, South Korea. This area has a wide intertidal zone that is mainly composed of clay and silt, with a tidal range of 6–7 m. The Hwang-do tidal flat is home to various invertebrates such as shellfish, crabs, and polychaetes, and is actively used for fishing activities,

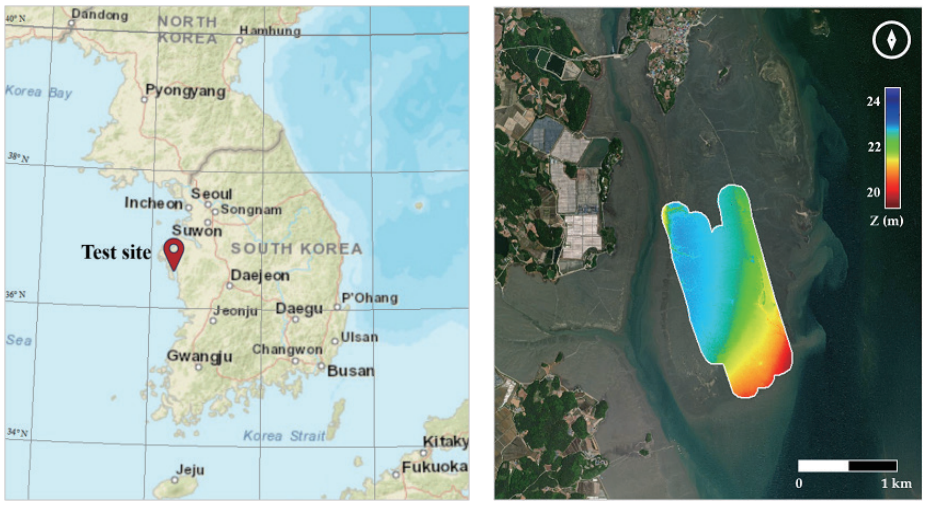

(a) (b)

Fig. 1. (Color online) Test site: (a) location and (b) aerial photograph and topography.

Table 1
Summary of test site.

Location	Taean-gun, Chungcheongnam-do, South Korea
Area	1.65 km^2
Spring tide range	7.33 m
Neap tide range	5.43 m
Mean sea level	3.98 m

such as shellfishing. It is also an important stopover site for migratory birds to find food and rest and an important natural ecosystem for various species of organisms. Our focus was on conducting bathymetry in areas where ABL surveys are challenging, specifically in shallow and turbid waters. Therefore, ABL data were collected during ebb tide when turbidity was high owing to currents, and a region with a water depth of less than 2 m was selected as the test area, as shown in Fig. 1(b).

2.2 Dataset

The bathymetric survey was conducted using the Seahawk system over a 21 km^2 area for a total flight time of 90 min. Seahawk utilizes a near-infrared (NIR) laser for topographic observation and a green laser for bathymetric surveying, and provides two green channel data (shallow green for shallow water surveying and deep green for deep water surveying).[20] In this study, since the test site is a shallow tidal flat area [Fig. 2(a)], the shallow green waveform data were used for the experiment. The ABL point cloud is generated from raw observation data using proprietary software, namely, the Lidar BAthymetry SyStem—Data processing (LBASSD); the data processing algorithms are not disclosed. The Seahawk system digitizes the received analog signal at 1.6 giga samples per second; thus, the time bin resolution of the waveform is 0.625 ns. The Seahawk individual waveform is recorded in 2,400 bins at 16 bits [0−65,536 digital number (DN)] per sample. In addition, we collected airborne topographic LiDAR (ATL) data during low tide on the same day to obtain ground truth for measuring the accuracy of the observed seabed location through ABL waveform processing [Fig. 2(b)]. The details of the two types of airborne LiDAR data are listed in Table 2. To analyze the turbidity environment of the test site and the characteristics of the ABL waveform according to turbidity, seawater turbidity was measured at nine spots from a ship [Fig. 2(c)]. Surface water was collected by direct sampling, and then the total suspended material (TSM) was measured through sampling filtration.

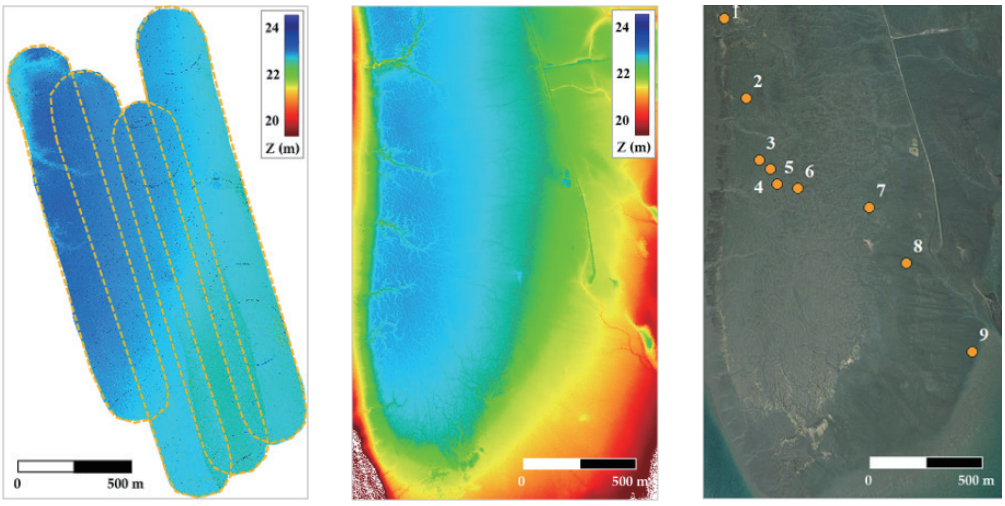

(a) (b) (c)

Fig. 2. (Color online) Test dataset: (a) airborne bathymetric LiDAR (ABL) data, (b) airborne topographic LiDAR (ATL) data as ground truth, and (c) turbidity measurement spots.

Table 2
Specifications of test datasets.

		Airborne bathymetric LiDAR	Airborne topographic LiDAR
System	Sensor	Seahawk	Terrain Mapper
	Laser wavelength	532 nm (shallow green/deep green) 1064 nm (NIR)	1064 nm
	Laser beam divergence	7 mrad (shallow green/deep green) 10.5 mrad (NIR)	0.23 mrad
	Pulse repetition rate	10 kHz	2000 kHz
	Field of view	20°	20–40°
	Weight	73 kg	48 kg
	Vertical accuracy	$\sqrt{0.5^2 + (0.013 \times depth)^2}$ (m)	< 5 cm 1 σ
Operation	Flight altitude	400 m	2,400 m
	Swath width	Up to 70% of flight altitude	Up to 70% of flight altitude
	Aircraft speed	140 knots	110 knots
	Acquisition time	Oct. 15, 2023 (Ebb tide)	Oct. 15, 2023 (Low tide)

3. Methods

The green laser beam of ABL propagates across the air–water interface, reaches the bottom, and then returns to the receiver, revealing the water surface and bottom positions through the peaks of the waveform.[21] A typical ABL waveform consists of the water surface return, water column backscatter, bottom return, and noise.[22] Individual components are separated through waveform decomposition, and the decomposed components are converted into points through position registration (Fig. 3).

To improve the seabed observation performance in the tidal flat area, we generated points through the following waveform processing process.

3.1 Preprocessing

First, waveforms with no received signal or those with defective signals were removed, and then preprocessing was performed on individual waveforms, including noise removal and actual signal range selection. Waveform data inevitably contain long-term, low-frequency background noise and short-term, high-frequency random noise. Background noise, typically related to solar radiation and detector dark current, is usually uniformly distributed and traditionally removed using a threshold.[23] However, in the west coast area where tidal activity is high, differences in the amount of background noise between waveforms may be present even during flight due to changes in solar reflectivity or turbidity during surveying. Therefore, a process for automatically estimating the amount of background noise for each individual waveform rather than a uniform threshold is necessary. The range in which the actual received signal is recorded in the waveform (signal range) occupies only a very small portion of the entire time record, and the main

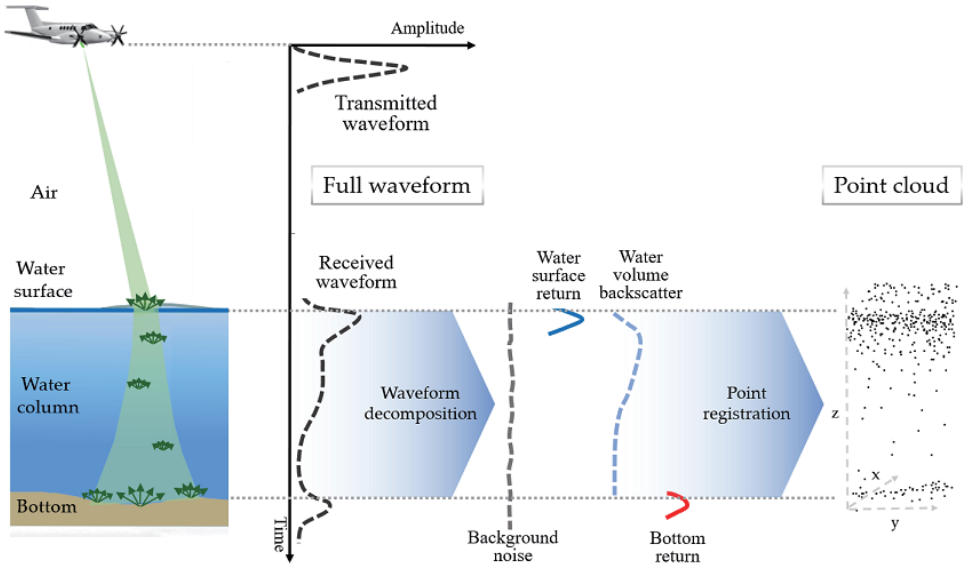

Fig. 3. (Color online) Data flow in airborne bathymetric LiDAR system.

contribution to the DN in most of the waveforms is background noise. Therefore, in this study, the mode of each waveform was considered as the amount of background noise, and the background noise was removed by differentiation:

$$y^* = y - mode(y), \tag{1}$$

where y and y^* are the original waveform and the waveform with background noise removed, respectively. Random noise is generally removed using low-pass filtering,[24] and in this study, smoothing through Gaussian filtering was applied to minimize the damage to the original waveform:

$$y_t' = \frac{1}{\sqrt{2\pi\sigma_G^2}} \sum_{k=1}^{w} y_k^* \exp\left(-\frac{(t-k)^2}{2\sigma_G^2}\right), \tag{2}$$

where y_t' is the Gaussian filtered value at time t, w indicates the number of waveform bins, and σ_G is the standard deviation of the Gaussian distribution. The larger σ_G is, the more smoothing is performed, and σ_G was empirically determined as 2 in this study.

Since the actual signal range is very limited in the waveform recorded in thousands of bins [Fig. 4(a)], we can increase computational efficiency by only performing analysis in the signal range and preventing the generation of outlier points caused by the false detection of noise in nonsignal ranges as peaks.[25] The signal range varies depending on the flight altitude, laser transmission angle, terrain altitude, and water depth. To distinguish between actual return signals and noise, the signal range is often determined on the basis of a random noise estimate of individual waveforms.[26,27] In this study, the standard deviation (σ_N) of the definite nonsignal range of the ABL system waveform was used as a standard for determining the signal range. The

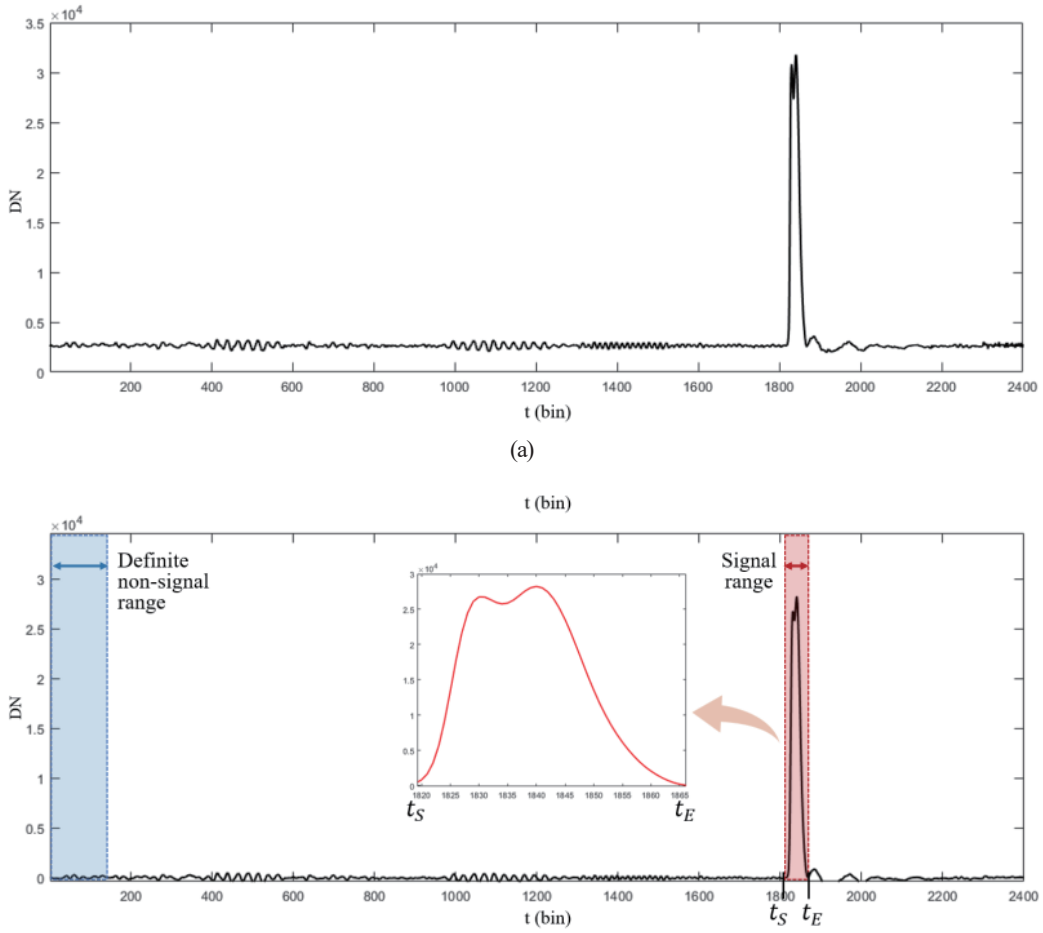

Fig. 4. (Color online) Example of preprocessing: (a) original waveform and (b) result of noise reduction and range determination.

Seahawk system records 2400 bins over 1.5 μs, with the first 0.1 μs (160 bins) considered as the nonsignal range for detector stabilization. The starting point (t_S) of the signal range is the point where the water surface reflection signal begins, the point at which the waveform amplitude DN significantly increases was selected, and the end point (t_E) was determined as the point where the amplitude becomes smaller than the DN of the starting point, as follows [Fig. 4(b)].

$$t_S = \min\left\{t \mid y'_{t+1} - y'_t > 3\sigma_N\right\} \tag{3}$$

$$t_E = \max\left\{t \mid y'_t > y'_{t_S}\right\} \tag{4}$$

3.2 Waveform decomposition

Generally, waveform decomposition techniques detect peaks (local maximum points) and use them as initial values for Gaussian model-based decomposition to perform multiple Gaussian model approximations, as in Eq. (5), where n, A_i, μ_i, and σ_i denote the number of Gaussian

models, amplitude, center position, and standard deviation of the ith Gaussian model, respectively.[28]

$$\hat{y} = \sum_{i=1}^{n} A_i \exp\left(-\frac{(t-\mu_i)^2}{2\sigma_i^2}\right) \tag{5}$$

The final decomposition performance is determined by the number and location of peaks initially detected. The Gaussian decomposition method is effective for waveforms with distinct peaks but struggles with ABL waveforms, where continuous scattering and overlapping Gaussian return signals cause a left-tilted signal.[25] Specifically, when the water depth is very shallow and the peaks of the surface and seabed reflection components overlap [Fig. 5(a)] or the seabed reflection component is very weak [Fig. 5(b)], each component may not be appropriately decomposed.

Therefore, in this study, progressive Gaussian decomposition (PGD),[29] which is suitable for waveform decomposition in shallow and turbid waters, was adopted and utilized in the experiment. PGD can improve the approximation accuracy of the decomposition model by gradually estimating and adding potential peak candidates to the initial peaks (Fig. 6). The PGD approach iteratively determines the optimal number of Gaussian models to decompose the waveform by starting with the number of detectable peaks and gradually increasing the number of models. The initial original peaks (OPs) are detected from the local maxima, and Gaussian curve fitting is performed using the Levenberg–Marquardt optimization algorithm. This process continues until the time difference between the OP and the estimated peak (EP) is within a specified threshold (τ) and the fitness is high. If the criteria are not met, further iterations add new initial values based on the most distant EPs from the OPs. The time threshold τ, which represents the acceptable temporal error in the waveform decomposition, is important for balancing fitting accuracy and computational efficiency. Setting τ too low can lead to overfitting and increased computational time, while setting it too high can reduce depth accuracy. In this study, τ was set to 5 bins, corresponding to a depth difference of approximately 0.34 m, on the

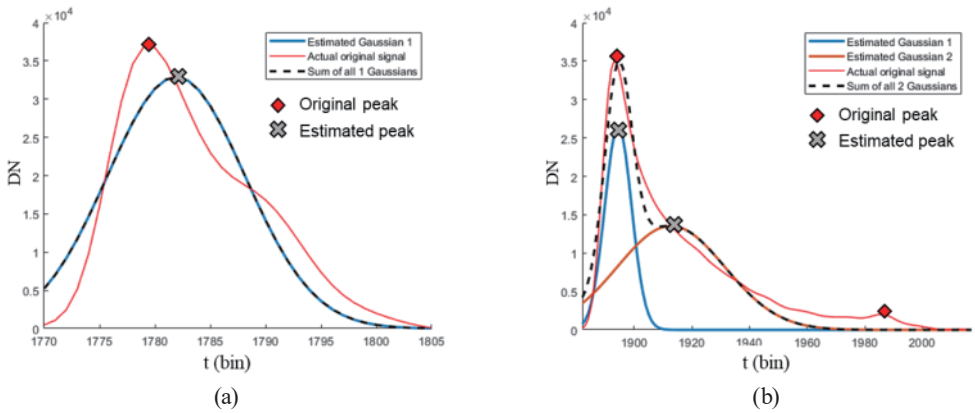

(a) (b)

Fig. 5. (Color online) Examples of general Gaussian decomposition results for ABL waveforms: (a) very shallow water and (b) deep water.

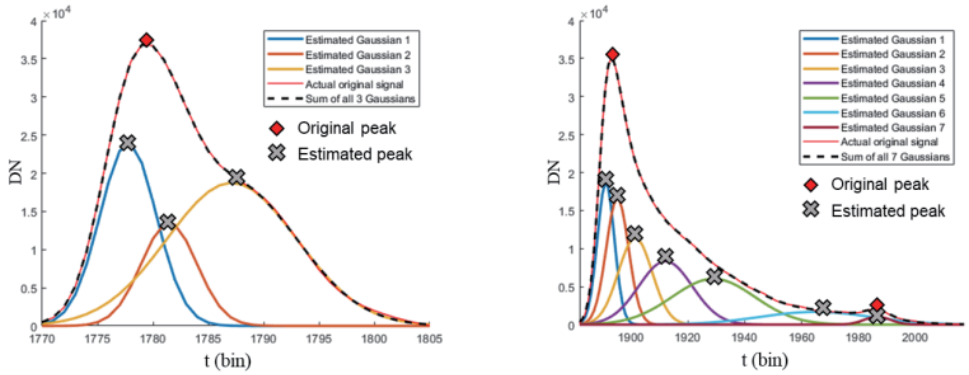

(a) (b)

Fig. 6. (Color online) Examples of progressive Gaussian decomposition (PGD) results for ABL waveforms: (a) very shallow water and (b) deep water.

basis of preliminary experiments and the Seahawk system's parameters. Figure 7 shows examples of the steps involved in the iterative PGD process for a waveform with two OPs and a water depth of 1.17 m. In the first and second iterations [Figs. 7(a) and 7(b), respectively], because some of the time distances from each OP to their nearest EP (e.g., Δt_{OP2}) exceed the threshold τ, potential peaks are gradually added to the initial values for the next iteration to perform optimization. The process continues until all time distances (Δt_{OPi}) are below τ [Fig. 7(c)]. The Gaussian components generated through the waveform decomposition were converted into points via geo-registration.

4. Results

4.1 Waveform types by turbidity

To investigate the effect of turbidity in tidal flat areas on ABL data, we analyzed the correlation between the turbidity values measured in the field and the ABL waveform features observed at the corresponding locations. After analyzing various waveform features, two features related to turbidity are listed in Table 3. The random noise was set to the standard deviation of the deterministic nonsignal range, as described in Sect. 3.1. The intensity area was used to estimate the attenuation of the return pulse energy and represent the total sum of the areas from the multiple Gaussian models of the decomposed components in each waveform. The results revealed that background noise had little correlation with turbidity, whereas random noise tended to increase with turbidity level. Figure 8 shows the results of the linear regression analysis between turbidity (TSM) and the corresponding waveform features. The positive correlation (R^2 = 0.63) between turbidity and ABL waveforms suggests that in the ABL waveforms obtained from highly turbid seawater, such as in mudflats, it may be more challenging to distinguish between actual return signals and noise [Fig. 8(a)]. The intensity domain showed a weak negative correlation (R^2 = 0.33) with turbidity, indicating that the reflected pulse energy tends to be attenuated more significantly as turbidity increases owing to underwater scattering [Fig. 8(b)]. To achieve more reliable trend and correlation analysis, a larger number of samples are required.

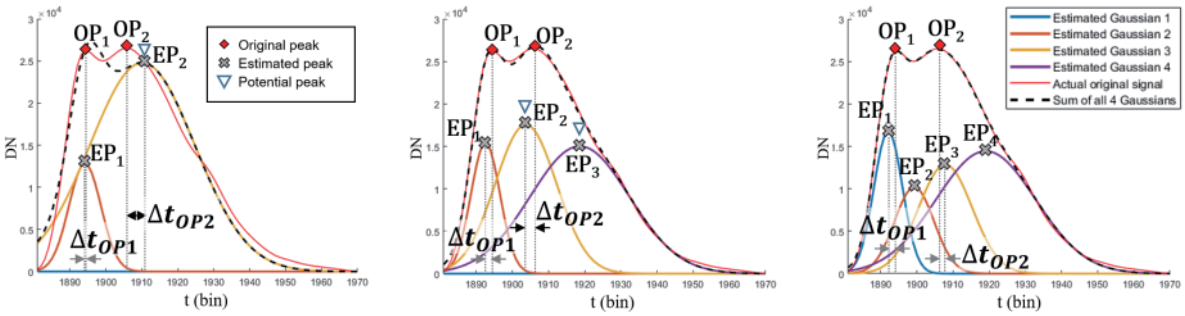

(a) (b) (c)

Fig. 7. (Color online) Iterative steps of PGD: (a) first iteration with original peaks (OPs), (b) second iteration with OPs and potential peaks, and (c) final decomposition result.

Table 3
Turbidity measurement and amount of waveform features.

Spot No.	TSM (mg/L)	Waveform feature	
		Random noise	Intensity area
1	14.27	123.41	598471
2	13.37	110.83	613131
3	36.85	262.79	516935
4	22.88	150.38	528031
5	24.72	122.34	513313
6	20.48	118.40	626553
7	8.09	102.31	577576
8	20.81	173.52	586084
9	8.72	138.84	985624

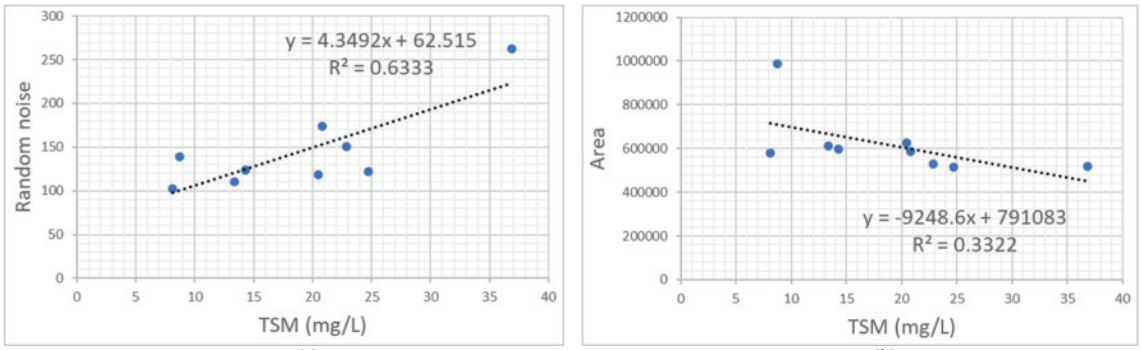

(a) (b)

Fig. 8. (Color online) Correlation between turbidity (TSM) and waveform features: (a) random noise and (b) intensity area.

Figure 9 shows examples of waveform shapes, signal ranges, and decomposition results for similar depths with varying levels of turbidity. This demonstrates that the ABL waveforms obtained from higher turbidity spots tend to have more random noise distributed throughout. Additionally, in highly turbid seawater, noise that could be mistaken for return peaks is often found in the later part of the signal range. Such waveform noise increases the likelihood of outliers (invalid points at lower altitudes than the seabed) occurring, making it even more critical

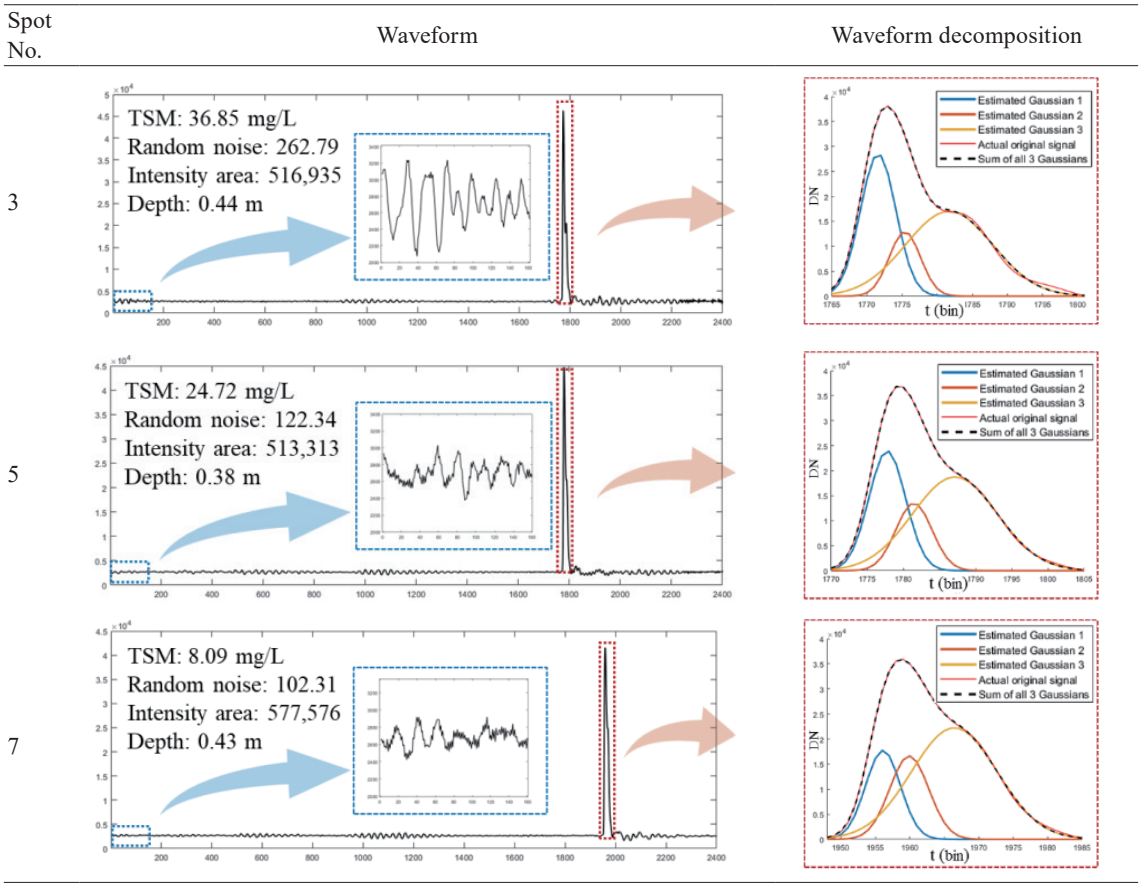

Fig. 9. (Color online) Examples of waveform and decomposition results under different levels of turbidity (spots 3, 5, and 7 in Table 3).

to accurately determine the signal range in high-turbidity areas. Figure 9 also demonstrates that waveforms with very shallow depths of approximately 0.4 m, where the bottom return peak is not detected, can be effectively decomposed using the proposed approach.

4.2 Seabed extraction comparison

To quantify the improvement in bathymetry performance using our approach, decomposed components were geo-registered to the point cloud and compared with a point cloud generated using LBASSD software. Because bathymetry performance relies on seabed observation, bottom points were manually extracted from point clouds generated by both our approach and LBASSD. As shown in Fig. 10, when processing the same ABL waveform data from test sites with depths of less than 2 m and high turbidity, LBASSD rarely extracted the bottom point. In contrast, the proposed approach successfully generated bottom points across almost the entire site, and the corresponding area and number of points are detailed in Table 4. This demonstrates that the approach effectively decomposed the shallow bottom component that overlapped closely with the water surface component.

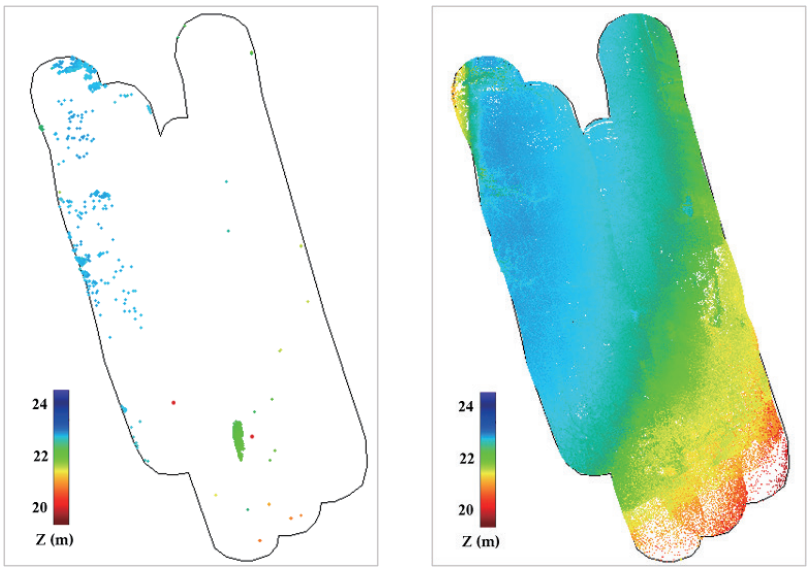

(a) (b)

Fig. 10. (Color online) Bottom point extraction results: (a) LBASSD and (b) proposed approach.

Table 4
Bottom point extractability results of LBASSD and proposed approach.

Method	Number of points	Area (m^2)	Max. depth (m)
LBASSD	1849	12464	0.86
Proposed approach	703988	1552016	2.15

4.3 Seabed accuracy evaluation

To evaluate the positional accuracy of the bottom points extracted using the proposed approach, we compared the locations of these extracted points with the ATL data obtained during low tide, serving as ground truth. The vertical errors (ΔZ) between the extracted bottom points and the ground truth surface are illustrated in Fig. 11. Overall, the results indicated that the extracted bottom points tend to be estimated at slightly higher elevations. The average error was 0.102 m, the standard deviation was 0.146 m, and the errors were distributed in a Gaussian shape, demonstrating that the proposed approach can achieve stable positional accuracy with a height precision exceeding International Hydrographic Organization (IHO) order 1b standards. Finally, Fig. 12 shows the 1-m-resolution DEM generated from results of this test.

5. Conclusions

The Korean Peninsula has extensive tidal flats with significant economic and potential value, which creates a strong demand for precise tidal flat terrain monitoring. In this study, we proposed an ABL waveform processing approach for the effective terrain surveying of tidal flats, where conducting depth measurements is challenging owing to their high turbidity and

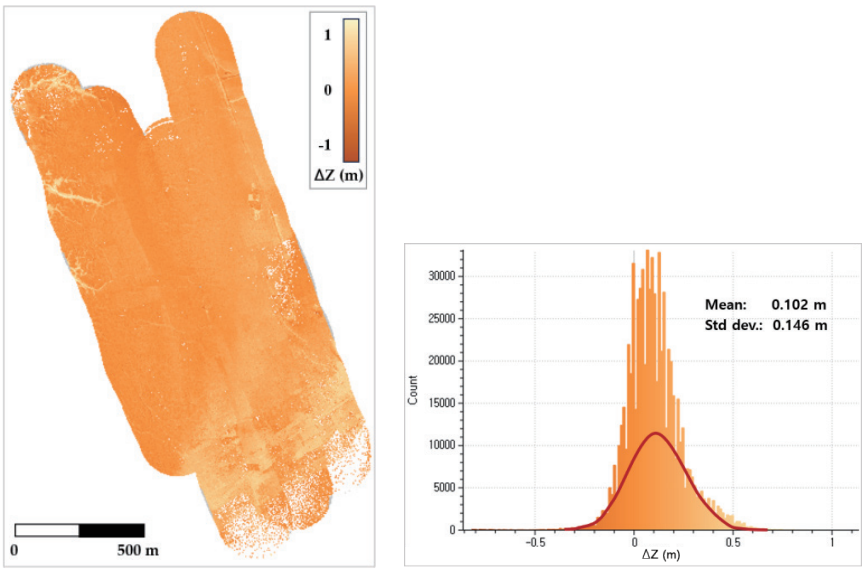

(a) (b)

Fig. 11. (Color online) Vertical error (Δ*Z*) between bottom points and ground truth: (a) Δ*Z* map and (b) Δ*Z* distribution.

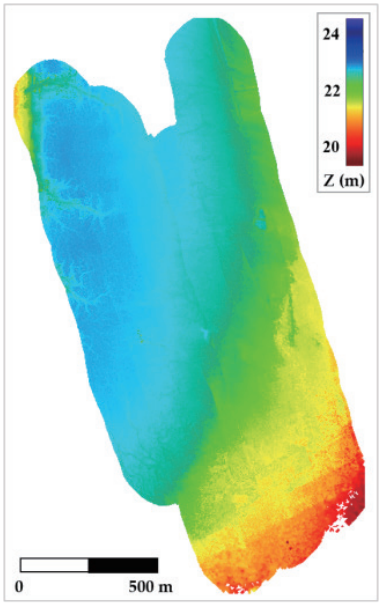

Fig. 12. (Color online) DEM generated from test results.

extremely shallow waters. We analyzed the correlation between the turbidity and ABL waveform data obtained from field measurements. The results revealed that a higher turbidity leads to an increase in irregular noise within the signal. To effectively handle this, it is crucial to predetermine the signal range where the actual return signal is recorded. Additionally, by adopting the PGD technique, we improved bottom extractability in extremely shallow waters (less than 2 m deep), where surface and bottom peaks overlap. However, since the number of turbidity

measurement points in the field was limited and the approach has not been validated across diverse regions, future work will focus on validation based on the data acquired from various tidal flat areas.

Acknowledgments

This research was supported by the Korea Institute of Marine Science & Technology (KIMST) funded by the Ministry of Oceans and Fisheries (RS-2023-00254717) and Basic Science Research Program through the National Research Foundation of Korea (NRF) funded by the Ministry of Education (No. 2021R1I1A3059263).

References

1 N. J. Murray, S. R. Phinn, M. DeWitt, R. Ferrari, R. Johnston, M. B. Lyons, N. Clinton, D. Thau, and R. A. Fuller: Nat. **565** (2019) 222. https://doi.org/10.1038/s41586-018-0805-8
2 Z. L. Chen and S. Y. Lee: Front. Mar. Sci. **9** (2022) 900896. https://doi.org/10.3389/fmars.2022.900896
3 Getbol, Korean Tidal Flats - UNESCO World Heritage: https://whc.unesco.org/en/list/1591/ (accessed June 2024).
4 K. S. Woo, S. S. Chun, and K. O. Moon: Geoheritage **12** (2020) 8. https://doi.org/10.1007/s12371-020-00445-8
5 J. H. Ryu, J. K. Choi, and Y. K. Lee: Ocean Coastal Manage. **102** (2014) 458. https://doi.org/10.1016/j.ocecoaman.2014.03.003
6 Y. Kang, J. Lei, M. Wang, G. Li, and X. Ding: Front. Mar. Sci. **10** (2023) 1163302. https://doi.org/10.3389/fmars.2023.1163302
7 S. Ma, N. Wang, L. Zhou, J. Yu, X. Chen, and Y. Chen: Remote Sens. **16** (2024) 685. https://doi.org/10.3390/rs16040685
8 H. Yang, M. Chen, X. Xi, and Y. Wang: Remote Sens. **16** (2024) 413. https://doi.org/10.3390/rs16020413
9 B. H. Choe and D. J. Kim: SAR Remote Sensing of Intertidal Flats in Korea: Remote Sensing of the Asian Seas, ed. V. Barale and M. Gade (Springer, Cham, 2019) p. 237. https://doi.org/10.1007/978-3-319-94067-0_13
10 B. J. Kim, Y. K. Lee, J. H. Ryu, S. Lee, and K. L. Kim: Proc. 2016 IEEE Int. Geoscience and Remote Sensing Symposium (IEEE, Beijing, 2016) 6699. https://doi.org/10.1109/IGARSS.2016.7730749
11 R. Brunetta, E. Duo, and P. Ciavola: Remote Sens. **13** (2021) 2322. https://doi.org/10.3390/rs13122322
12 Y. Li, Y. Wu, Z. Sun, D. Zhao, C. Yu, Y. Li, G. You, Z. Kong, X. Xi, and L. Lei: J. Coastal Conserv. **27** (2023). https://doi.org/10.1007/s11852-023-00951-1
13 H. Zhang, L. Wang, Y. Zhao, J. Cao, and M. Xu: Front. Mar. Sci. **9** (2022) 871156. https://doi.org/10.3389/fmars.2022.871156
14 H. Kim, Y. Kim, and J. Lee: KSCE J. Civ. Eng. **24** (2020) 2767. https://doi.org/10.1007/s12205-020-2336-8
15 A. Szafarczyk and C. Toś: Sens. **23** (2023) 292. https://doi.org/10.3390/s23010292
16 C. Wang, Q. Li, Y. Liu, G. Wu, P. Liu, and X. Ding: ISPRS J. Photogramm. Remote Sens. **101** (2015) 22. https://doi.org/10.1016/j.isprsjprs.2014.11.005
17 Z. Pan, C. Glennie, P. Hartzell, J. C. Fernandez-Diaz, C. Legleiter, and B. Overstreet: Remote Sens. **7** (2015) 5133. https://doi.org/10.3390/rs70505133
18 M. S. Andersen, Á. Gergely, Z. Al-Hamdani, F. Steinbacher, L. R. Larsen, and V. B. Ernstsen: Hydrol. Earth Syst. Sci. **21** (2017) 43. https://doi.org/10.5194/hess-21-43-2017
19 D. Mader, K. Richter, P. Westfeld, and H. Maas: PFG- J. Photogramm. Remote Sens. Geoinf. Sci. **89** (2021) 139. https://doi.org/10.1007/s41064-021-00147-y
20 H. Kim, G. H. Tuell, J. Y. Park, E. Brown, and G. We: J. Coast. Res. **91** (2019) 376. https://doi.org/10.2112/SI91-076.1
21 K. Saylam, J. R. Hupp, A. R. Averett, W. F. Gutelius, and B. W. Gelhar: Int. J. Remote Sens. **39** (2018) 2518. https://doi.org/10.1080/01431161.2018.1430916
22 X. Zhao, J. Zhao, H. Zhang, and F. Zhou: Remote Sens. **10** (2018) 247. https://doi.org/10.3390/rs10020247
23 F. Yang, C. Qi, D. Su, S. Ding, Y. He, and Y. Ma: Int. J. Appl. Earth Obs. Geoinf. **109** (2022) 102788. https://doi.org/10.1016/j.jag.2022.102788

24 L. Huang, Q. Kemao, B. Pan, and A. K. Asundi: Opt. Laser Eng. **48** (2010) 141. https://doi.org/10.1016/j.optlaseng.2009.04.003
25 K. Guo, W. Xu, Y. Liu, X. He, and Z. Tian: Remote Sens. **10** (2017) 35. https://doi.org/10.3390/rs10010035
26 B. Jutzi and U. Stilla: ISPRS J. Photogramm. Remote Sens. **61** (2006) 95. https://doi.org/10.1016/j.isprsjprs.2006.09.001
27 S. Xing, D. Wang, Q. Xu, Y. Lin, P. Li, L. Jiao, X. Zhang, and C. Liu: Sens. **19** (2019) 5065. https://doi.org/10.3390/s19235065
28 C. Mallet and F. Bretar: ISPRS J. Photogramm. Remote Sens. **64** (2009) 1. https://doi.org/10.1016/j.isprsjprs.2008.09.007
29 H. Kim, M. Jung, J. Lee, and G. Wie: Appl. Sci. **13** (2023) 10939. https://doi.org/10.3390/app131910939

About the Authors

Hyejin Kim received her B.S. and Ph.D. degrees from Seoul National University, South Korea, in 2001 and 2020, respectively. From 2021 to 2023, she was a chief researcher at Mokpo National University, South Korea. Since 2023, she has been a senior researcher at Konkuk University, South Korea. Her research interests are in ABL data processing and coastal feature extraction. (evervicky@konkuk.ac.kr)

Jaebin Lee received his B.S. degree from Yonsei University, South Korea, in 2000 and his Ph.D. degree from Seoul National University, South Korea, in 2008. Since 2009, he has been a professor at Mokpo National University. His research interests are in the full-waveform processing and classification of ABL data. (lee2009@mnu.ac.kr)